

Vacancy localization effects on MX_2 transition metal dichalcogenides: a systematic ab-initio study

Rafael L. H. Freire¹,* Felipe Crasto de Lima¹,† and Adalberto Fazzio¹,‡
Illum School of Science, CNPEM, 13083-970 Campinas, Brazil
 (Dated: May 9, 2022)

Two-dimensional transition metal dichalcogenides (MX_2) vacancy formation energetics is extensively investigated. Within an ab-initio approach we study the MX_2 systems, with $\text{M}=\text{Mo}$, W , Ni , Pd and Pt , and $\text{X}=\text{S}$, Se , and Te . Here we classify that chalcogen vacancies are always energetic favorable over the transition metal ones. However, for late transition metals Pd $4d$, and Pt $5d$ the metal vacancy are experimentally achievable, bringing up localized magnetic moments within the semiconducting matrix. By quantifying the localization of the chalcogen vacancy states we evidentiate that it rules the intra- and inter-vacancy interactions that establish both the number of vacancy states neatly lying within the semiconducting gap, as well as its electronic dispersion and SOC splitting. Combining different vacancies and phase variability 1T and 1H of the explored systems allow us to construct a guiding picture for the vacancy states localization.

I. INTRODUCTION

Defects on materials, and particularly atomic vacancies, arises as a possible route for an experimental control of properties [1, 2]. Although the plethora of possible materials defects, ranging from localized to extended, even the elementary structural defect (atomic single vacancy) allow for an complex phenomena to arise, for instance ruling the molecular self-assemblies over two-dimensional (2D) substrates [3]. Additionally, controlling such punctual defects on the precise manipulation of vacancies have allowed the construction and engineering of metamaterials [4, 5]. In order to further explore materials modification through vacancies, a clear picture of the intrinsic vacancy properties are needed.

Two-dimensional transition metal dichalcogenides (TMD's) are an interesting class of materials holding tremendous potential for applications, encompassing catalysis [6, 7], (opto)electronics [8–10], spintronics [10, 11], magnetism [12] and energy storage [13, 14]. Particularly, the presence of defects in 2D-TMD materials can directly impact their properties, causing a variety of phenomena that could be either detrimental acting like carrier scattering and localization sites [15] or beneficial as is the case of active catalytic sites, and magnetic orderings [16]. Furthermore, spin-orbit effects on those materials combined with point defects may give rise to interesting phenomena such as giant magnetoresistance [17], topological phases [18], all of which could be employed on spintronic devices. Additionally, recent experimental works have shown that the localization character of the vacancy states induces electronic transport [19], and magnetism ordering on transition metal vacancies [20].

In this study, we perform ab-initio calculations based on the density functional theory to clarify and quantify the localization character of vacancies states on TMD. We considered the pristine and defected MX_2 2D systems (for $\text{M} = \text{Ni}$, Mo , Pd , W , and Pt , and $\text{X} = \text{S}$, Se , and Te) in their 1H , 1T , and $1\text{T}'$ phases (see Fig. 1). We highlight the most stable structural phase and most

stable vacancies (of metals or chalcogen). We present an analysis of the localization nature of such vacancy states and their consequences to the energetic, electronic, and magnetic properties.

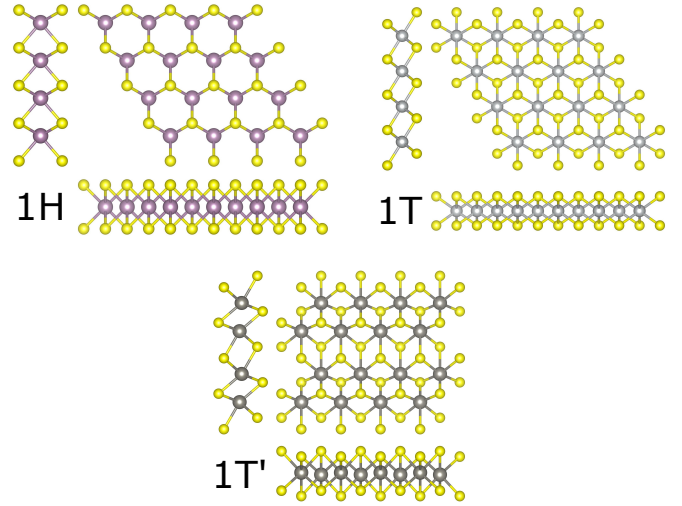


FIG. 1. 1H , 1T , and $1\text{T}'$ MX_2 2D structural phases.

II. COMPUTATIONAL APPROACH

Spin-polarized calculations based on density functional theory (DFT) [21, 22] were performed within the semi-local exchange-correlation functional proposed by Perdew–Burke–Ernzerhof (PBE) [23]. To treat the long range dispersion van der Waals (vdW) interactions, the pairwise D3 correction framework as proposed by Grimme were considered [24, 25].

For the total energies, $E_{tot}^{\text{DFT}+\text{vdW}}$, the electron-ion core interactions were considered within the projector augmented wave (PAW) method [26, 27], as implemented in the Vienna *Ab-Initio* Simulation Package (VASP) [28, 29]. The spin-orbit coupling was considered

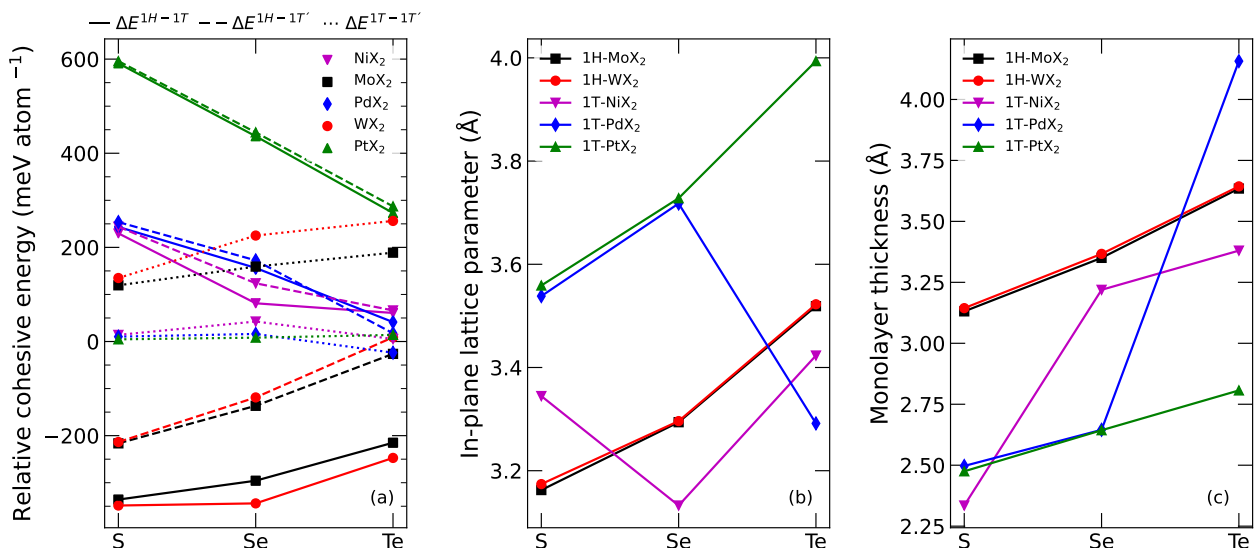


FIG. 2. (a) Relative cohesive energies for all pristine systems and structural parameters, namely (b) in-plane lattice and (c) monolayer thickness, for the most stable MX_2 structures.

for the most stable configuration. For all calculations, cutoff energy for the plane-wave expansion of the Kohn–Sham orbitals was set to 520 eV, under an energy convergence parameter of 10^{-6} eV, with all atoms relaxed until the atomic forces on every atom were smaller than 10^{-3} eV \AA^{-1} . A uniform $4 \times 4 \times 1$ k-point mesh was considered for the Brillouin zone (BZ) integration, while a thinner mesh grid, $8 \times 8 \times 1$, was used for Density of States (DOS) calculations.

The 2D in-plane lattice parameters (a and b) were optimized for a 1×1 unit cell with a fixed vacuum distance (c) of at least 20 \AA . Those lattice parameters were used to build up the pristine and single vacancy 5×5 and 3×3 unit cells to the 1H and 1T (1T') structures, with the former being large enough to avoid spurious interaction between periodic images.

III. RESULTS AND DISCUSSION

A. Structural Stability

To analyze the structural stability of the pristine structures, we calculated the cohesive energies – being the total energy difference between the material and each isolated atom – for the 1H, 1T, and, 1T' phases. To better present the relative stability of one phase against each other, we evaluated their relative cohesive energy, namely ΔE^{1H-1T} , $\Delta E^{1H-1T'}$, and $\Delta E^{1T-1T'}$, as shown in Fig. 2 (a). That is, $\Delta E^{1H-1T} > 0$ indicates the 1H phase is more stable than the 1T phase, and similarly to the other relative energies. As one can see, the negative values for 1H-1T (200–400 meV atom $^{-1}$) and 1H-1T' (0–200 meV atom $^{-1}$) for MoX_2 and WX_2 indicate the 1H phase as the most stable, with this stability decreasing

with the increase of the chalcogen atomic radius. Despite the slightly positive values observed for NiX_2 , PdX_2 , and PtX_2 , the cohesive energy differences point to the 1T phase as the most stable, with the 1T-1T' differences being close to zero. Although the calculation started in the 1T' phase, after relaxation it converged barrierlessly into the 1T phase.

In general, the 1T phase has larger in-plane lattice parameters [Fig. 2(b)] with a smaller monolayer thickness as compared to the 1H phase and its more open structure (hexagonal holes). Consequently the monolayer thickness [Fig. 2(c)] decreases as the chalcogen planes move down to stabilize the equilibrium covalent bond length. In the 1H phase, the in-plane lattice parameter and monolayer thickness increase going from S \rightarrow Te, as a result of accommodating larger chalcogen atoms within the structure. In the case of the 1T phase, only PtX_2 follows a similar trend as the 1H phase. On the other hand, 1T- NiX_2 and 1T- PdX_2 undergo larger relaxation effects.

B. Vacancy formation energy

After pristine systems optimization, we built up a 5×5 defective monolayers considering the most stable phases for each system, namely the 1H phase for MoX_2 and WX_2 systems, and the 1T phase for NiX_2 , PdX_2 , and PtX_2 . Both native point defects comprising chalcogen (V_X) and transition metal (V_M) vacancies were considered with the vacancy-vacancy distances in the 1H (1T) around 15.8–17.6 \AA (15.7–20.0 \AA).

In Figure 3, we present the formation energies, E_f , for both M and X vacancies for the selected systems, evaluated according to

$$E_f = E_{def}^{MX_2} - (E_{pristine}^{MX_2} - E_{M,X}^{free-atom}), \quad (1)$$

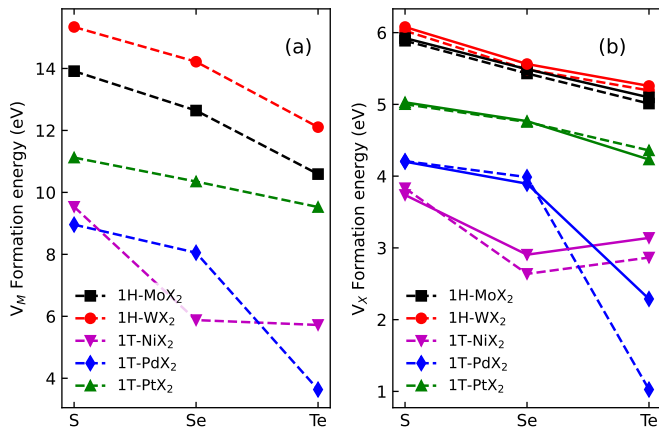


FIG. 3. Native point defect formation energies. (a) is the transition metal vacancy defect, and (b) the chalcogen defect. In the latter, we show formation energies for both 5×5 (dashed lines) and 3×3 (solid lines) supercell sizes.

in which $E_{def}^{MX_2}$ is the energy of the defected system; $E_{pristine}^{MX_2}$ is the energy of the pristine system; and $E_{M,X}^{free-atom}$ is free-atom energy of the corresponding atom M or X which generates the vacancy defect.

As indicated in Fig. 3 both formation energies are endothermic, with the formation energies of transition metal vacancies [Fig. 3 (a)] are higher than that for the chalcogen [Fig. 3 (b)]. Considering the different structure phases, one can realize that the defect formation energies in the 1T phase are always smaller than those for the 1H phase. Particularly, Ni and Pd systems with the heavier chalcogen (Se and Te) present transition metal vacancy formation energy close to the scale values of the chalcogen vacancies, indicating a possible occurrence of such defects (although less favorable than X-vacancies). Additionally, for the X-vacancies, we present the formation energy in a 3×3 supercell, i.e. increased vacancy density, where the interaction between neighboring vacancies is greater. As we can see the NiSe₂, NiTe₂, and PdTe₂ structures present a larger difference in the chalcogen vacancy formation energy in the 3×3 cell when compared with the lower vacancy density case. As we will show in the next sections, such behavior is a consequence of the more delocalized nature of the vacancy states in those systems.

C. Band structure analysis

In Fig. 4, we show a defected 5×5 supercell model for both 1H and 1T structures alongside their characteristic band structures with and without spin-orbit coupling. The introduction of the chalcogen vacancy leads to three defect states, corresponding to the three transition metal dangling bonds over the vacancy environment. The triangular C_{3v} local environment split the dangling bond states into E and A_1 irreducible representations.

Additionally, the interaction of those three intra-vacancy dangling bonds in the 1H structure is larger than the 1T, given the remaining chalcogen coupling those TM. That is, this stronger coupling leads to a large energy separation between the E and A_1 irreducible representation. Such an interaction picture leads to three vacancy states on the 1T phase neatly lying on the system energy gap (E and A_1 states), while for the 1H phase the two E states remain in the energy gap, with the A_1 state being within the valence bands. Additionally to this picture, the SOC effect has a role in splitting the E states into two sets. Such value of splitting is directly related to the SOC contribution in each system. In Fig. 4(c) we show the SOC splitting value at Γ for the lower vacancy density system (5×5 cell). Here, the TM atom mostly rules the SOC contribution, with a lower variance of the value with the chalcogen atom. Such variance is higher for WX₂ systems, 50 meV, while lower for MoX₂ systems, 25 meV. For the 5d TM, the 1H tungsten phases present the highest splitting, with the WS₂ reaching close to 0.2 eV, followed by the 1T Pt phases. For the 4d TM similar trend is observed with the 1H Mo phases presenting higher SOC splitting than Pd 1T phases. Interestingly, going towards a higher vacancy density, where the interaction between adjacent vacancy states becomes important, the SOC trend is altered. First note that the vacancy states become dispersive, Fig. 4(b) right panels. The combined effect of the dispersion of the bands and SOC, induce a higher gap opening at the Γ point for the 1T phases compared with the 1H ones. For instance, such a gap goes over 0.3 eV for PtTe₂, with a dependence of the chalcogen atom being more accentuated. The dependence arises given the indirect coupling between adjacent vacancy states being ruled by the TMD matrix [18]. To further explore such indirect coupling we quantify the localization of such vacancy states.

D. (De)Localization

To take into account (de)localization effects due to the vacancy formation, we characterized the defective systems through the inverse participation ratio (IPR) [30] given by

$$\text{IPR}_{n,k} = \frac{\sum_{i=1}^N |\langle i | \psi_{n,k} \rangle|^4}{\left(\sum_{i=1}^N |\langle i | \psi_{n,k} \rangle|^2 \right)^2}, \quad (2)$$

in which $\langle i | \psi_{n,k} \rangle$ was taken as the sum of the orbital projected KS eigenstate for each site/atom i , such that N is the total number of atoms in the cell. Thus, for a fully localized state the IPR should be one, while a delocalized one corresponds to the limit $\text{IPR} = 1/N$. In Fig. 5, we show the IPR values for each $|\psi_{n,k}\rangle$ state as a function of its eigenvalue, for the most stable phases for chalcogen vacancies. It is worth pointing out that

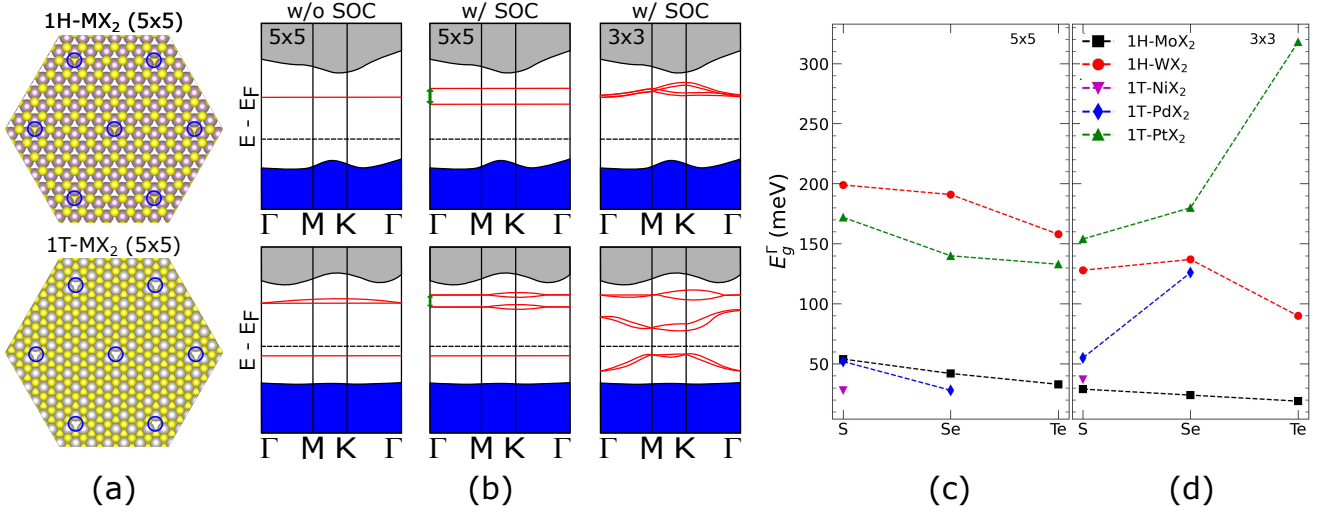


FIG. 4. (a) 5×5 defect supercell for 1H and 1T phases as indicated; (b), the universal schematic of band structure of each semiconducting phase, respectively, with and without spin-orbit corrections. The green arrows indicated spin-orbit splitting of the corresponding k -point; (c) Spin-orbit splittings calculated for both 3×3 and 5×5 defect supercells. E_g^Γ is the spin-orbit splitting at the Γ point.

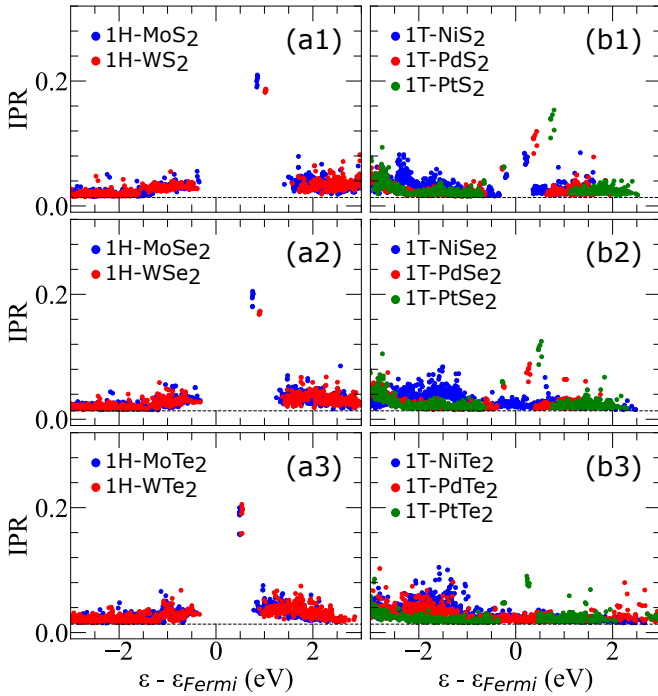


FIG. 5. Inverse participation ratio (IPR) as a function of the Bloch wavefunction ($|\psi_{n,k}\rangle$) energy. (a1)-(a3) The IPR for 1H-MX₂ phases with M=Mo, and W and (b1)-(b3) The IPR for 1T-MX₂ phases, with M=Ni, Pd, and Pt from S to Te, respectively

those defective systems are in general semiconducting, with exception of NiSe₂, NiTe₂, and PdTe₂, which are metallic, as indicated by the energy gap at Fig. 5 x -axis.

In the semiconducting cases, the localized states that appear within the gap corresponding to the va-

cancy states as depicted in Fig. 4. The 1H phases present a slightly larger IPR when compared to the 1T phases. Taking the 1H phase as an example [Fig. 5(a1)-(a3)], after the chalcogen vacancy formation, if (in the ideal case) only the three transition metal orbitals ($|M_i\rangle$) neighboring the vacancy contributes equally (with $\langle M_i | \psi_{vac-state} \rangle = a$) to the localization, we have $IPR = 3a^4 / (3a^2)^2 = 1/3$. That is, the localization limit is $1/3$ at the chalcogen vacancy surroundings. As observed the IPR values are around 0.20 which is close to the ideal limit, being reduced due to the spread of the vacancy states to hybridized neighboring orbitals. The same IPR limit ($IPR=1/3$) is valid for the 1T structures [Fig. 5(b1)-(b3)]. However, despite the vacancy states being within the bandgap, the values observed are slightly small, lying around $IPR=0.15$. In this case, an enhanced environment interaction is observed. To better visualize it, in Fig. 6 we show the vacancy states squared wave function (partial charge density) of MoS₂ and PtSe₂ with S and Se vacancy, which respectively present an IPR of 0.2 and 0.1. The 1T phase forms a pyramidal-like configuration [see Fig. 6 (b)], in which the localized state spreads to opposite surface chalcogen atoms neighboring the dangling bond Pt atom. On the other hand, the 1H phase LDOS [see Fig. 6(a)] are mostly localized in the M atoms close to the vacancy. Thus, the IPR for these localized states decreases for the 1T phase as compared to the 1H one. The spatial distribution of those vacancy states, although with different spreads follow the same three-fold symmetry of the vacancy structure.

In the light of the quantification of the localization through the IPR, the chalcogen vacancy formation energy and the band structure dependence of the vacancy density can be readily explained. For instance, given the more localized nature of Mo, W, and Pt vacancy states

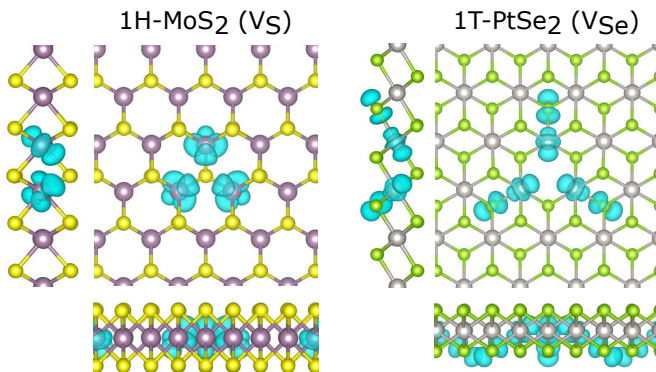


FIG. 6. LDOS for the chalcogen-defected systems (a) 1H-MoS₂ and (b) 1T-PtSe₂, with the same isosurface of 0.007 e/Å³

all above IPR= 0.1, dictates that the adjacent vacancies will have lower interaction not changing the formation energy significantly. However Ni and Pd, with their IPR < 0.1 indicate a stronger interaction between adjacent vacancies reducing the formation energy for higher vacancy densities. Particularly, for the 1T phases with Te [Fig. 5(b3)] which presents the lower IPR values for the vacancy states, presents also the greater variability on the chalcogen vacancy formation energy, see Fig. 3(b). A similar analysis can be done following the band structure. Here, the 1T phases allowing a longer range of interaction between adjacent vacancies leads to higher dispersive states when compared with the 1H structure [Fig. 4(b)]. Here the localization of the chalcogen vacancy states leads to the interpretation of their interaction, additionally, TM vacancies can also lead to localized magnetic effects.

E. Magnetism

Although less energetically favorable, TM vacancies can also be found on TMD, where the introduction of such vacancies can induce a local net magnetic moment. In Table I we summarize the systems presenting a net magnetic moment after a TM vacancy is formed, while the ones not present on the table did not present any magnetic properties. After the TM vacancy is formed, localized magnetic moments arise on the neighboring chalcogen atoms. Here a ferromagnetic (FM) phase can be stabilized for some explored systems, being the only observed phase for the 1H structure. Interestingly, some of the 1T systems can present an antiferromagnetic (AFM) arrange of such chalcogen magnetic moments, which can be more stable than the ferromagnetic, as already observed for 1T-PtSe₂ [12]. Aware of this behavior, we probed this antiferromagnetic configuration for our 1T-based based systems. The systems which presented a possible antiferromagnetic phase were 1T-NiS₂, 1T-PdS₂, 1T-PdSe₂, 1T-PtS₂, and 1T-PtSe₂. However,

as shown in Table I, for Ni- and Pd-based systems the antiferromagnetic phase ($\Delta E^{AFM-FM} < 0$) were not the most stable. On the other hand, for Pt-based systems we found more stable antiferromagnetic phases for 1T-PtS₂ and 1T-PtSe₂ systems with an energy difference about -54 meV/vacancy, and -33 meV/vacancy, respectively. That is, such values for the AFM phase together with the FM of 1T-PdSe₂ [with $\Delta E^{AFM-FM} = 43$ meV/vacancy], dictates such magnetic configurations to be robust close to the ambient temperature.

TABLE I. Magnetic moments, m (μ_B), induced in the most stable phases with the introduction of vacancies. The last column, ΔE^{AFM-FM} (meV/vacancy), is the energy difference between the antiferromagnetic (AFM) and ferromagnetic (FM) phases, with $\Delta E^{AFM-FM} < 0$ indicating the AFM phase being more stable.

MX ₂	vacancy	m	ΔE^{AFM-FM}
1H-MoSe ₂	Mo	4.00	-
1H-MoTe ₂	Mo	2.00	-
1H-WTe ₂	W	1.96	-
1T-NiS ₂	Ni	4.00	19
1T-PdS ₂	Pd	4.00	17
1T-PdSe ₂	Pd	4.00	43
1T-PtS ₂	Pt	4.00	-54
1T-PtSe ₂	Pt	4.00	-33

IV. CONCLUSIONS

We systematically investigated the energetic and electronic properties of a series of two-dimensional transition metal dichalcogenides (MX₂, with M=Ni, Mo, Pd, W, and Pt; and X=S, Se, and Te) presenting native point defects, namely chalcogen and transition metal vacancies, in different structural phases. Here, we found the chalcogen vacancy as the most stable for all systems, with lower formation energy in the 1T phase (Ni, Pd, and Pt systems) than those in the 1H phase (Mo and W systems). However, transition metal vacancies can still be found under experimental conditions. In this sense, our results show the appearance of localized magnetic moments induced by metal vacancies for 1T-PtS₂ and 1T-PtSe₂ that could be applied to design new 2D magnets. Furthermore, we have explored the localization effects of the chalcogen vacancy states. Such, localized states give rise to three energy levels that can be neatly lying on the TMD matrix energy gap. Here the localization strength, quantified by the defect states inverse participation rate, is shown to be greater in the 1H phases. This leads to both (i) a stronger repulsion between the three defect states (with C_{3v} , E and A_1 irreducible representations) increasing the gap between E and A_1 states, and (ii) giving rise to lower dispersion for higher vacancy densities, that is, present a lower vacancy-vacancy interaction. For the 1T phases, the more delocalized nature of the vacancy

states gives rise to a stronger hopping-like interaction between adjacent vacancies. Additionally, we have shown that vacancy-vacancy interactions (given by their localization) ruled not only the materials band dispersion but also the SOC splittings. This investigation brings insightful discussions on the nature of energetic and electronic effects of vacancy defects within the different 2D-TMD material phases and vacancy concentration.

ACKNOWLEDGMENTS

The authors acknowledge financial support from the Brazilian agencies FAPESP (grant 20/14067-3 and 17/02317-2), INCT-Nanomateriais de Carbono, and Laboratório Nacional de Computação Científica for computer time.

* rafael.freire@lnnano.cnpem.br

† felipe.lima@ilum.cnpem.br

‡ adalberto.fazzio@ilum.cnpem.br

¹ Qijie Liang, Qian Zhang, Xiaoxu Zhao, Meizhuang Liu, and Andrew T. S. Wee, “Defect Engineering of Two-Dimensional Transition-Metal Dichalcogenides: Applications, Challenges, and Opportunities,” *ACS Nano* **15**, 2165–2181 (2021).

² Massimiliano Cavallini and Denis Gentili, “Atomic Vacancies in Transition Metal Dichalcogenides: Properties, Fabrication, and Limits,” *ChemPlusChem* **87**, e202100562 (2022).

³ X. Lin, J. C. Lu, Y. Shao, Y. Y. Zhang, X. Wu, J. B. Pan, L. Gao, S. Y. Zhu, K. Qian, Y. F. Zhang, D. L. Bao, L. F. Li, Y. Q. Wang, Z. L. Liu, J. T. Sun, T. Lei, C. Liu, J. O. Wang, K. Ibrahim, D. N. Leonard, W. Zhou, H. M. Guo, Y. L. Wang, S. X. Du, S. T. Pantelides, and H.-J. Gao, “Intrinsically patterned two-dimensional materials for selective adsorption of molecules and nanoclusters,” *Nature Materials* **16**, 717–721 (2017).

⁴ Giang D. Nguyen, Liangbo Liang, Qiang Zou, Mingming Fu, Akinola D. Oyedele, Bobby G. Sumpter, Zheng Liu, Zheng Gai, Kai Xiao, and An-Ping Li, “3D Imaging and Manipulation of Subsurface Selenium Vacancies in PdSe₂,” *Phys. Rev. Lett.* **121**, 086101 (2018).

⁵ Zhe Li, Hsin-Yi Tiffany Chen, Koen Schouteden, Koen Lauwaet, Ewald Janssens, Chris Van Haesendonck, Gianfranco Pacchioni, and Peter Lievens, “Lateral Manipulation of Atomic Vacancies in Ultrathin Insulating Films,” *ACS Nano* **9**, 5318–5325 (2015).

⁶ Damien Voiry, Jieun Yang, and Manish Chhowalla, “Recent Strategies for Improving the Catalytic Activity of 2D TMD Nanosheets Toward the Hydrogen Evolution Reaction,” *Advanced Materials* **28**, 6197–6206 (2016).

⁷ Charlie Tsai, Hong Li, Sangwook Park, Joonsuk Park, Hyun Soo Han, Jens K. Nørskov, Xiaolin Zheng, and Frank Abild-Pedersen, “Electrochemical generation of sulfur vacancies in the basal plane of MoS₂ for hydrogen evolution,” *Nature Communications* **8**, 15113 (2017).

⁸ Rui Cheng, Dehui Li, Hailong Zhou, Chen Wang, Anxiang Yin, Shan Jiang, Yuan Liu, Yu Chen, Yu Huang, and Xiangfeng Duan, “Electroluminescence and Photocurrent Generation from Atomically Sharp WSe₂/MoS₂ Heterojunction p-n Diodes,” *Nano Letters* **14**, 5590–5597 (2014).

⁹ Xu Cui, Gwan-Hyoung Lee, Young Duck Kim, Ghidewon Arefe, Pinshane Y. Huang, Chul-Ho Lee, Daniel A. Chenet, Xian Zhang, Lei Wang, Fan Ye, Filippo Pizzocchero, Bjarke S. Jessen, Kenji Watanabe, Takashi Taniguchi, David A. Muller, Tony Low, Philip Kim, and James Hone, “Multi-terminal transport measurements of MoS₂ using a van der Waals heterostructure device platform,” *Nature*

Nanotechnology **10**, 534–540 (2015).

¹⁰ Qing Hua Wang, Kouros Kalantar-Zadeh, Andras Kis, Jonathan N. Coleman, and Michael S. Strano, “Electronics and optoelectronics of two-dimensional transition metal dichalcogenides,” *Nature Nanotechnology* **7**, 699–712 (2012).

¹¹ A. Avsar, H. Ochoa, F. Guinea, B. Özyilmaz, B. J. van Wees, and I. J. Vera-Marun, “Colloquium: Spintronics in graphene and other two-dimensional materials,” *Rev. Mod. Phys.* **92**, 021003 (2020).

¹² Ahmet Avsar, Cheol-Yeon Cheon, Michele Pizzocchero, Mukesh Tripathi, Alberto Ciarrocchi, Oleg V. Yazyev, and Andras Kis, “Probing magnetism in atomically thin semiconducting PtSe₂,” *Nature Communications* **11**, 4806 (2020).

¹³ Guodong Du, Zaiping Guo, Shiquan Wang, Rong Zeng, Zhixin Chen, and Huakun Liu, “Superior stability and high capacity of restacked molybdenum disulfide as anode material for lithium ion batteries,” *Chem. Commun.* **46**, 1106–1108 (2010).

¹⁴ Kun Chang and Weixiang Chen, “l-Cysteine-Assisted Synthesis of Layered MoS₂/Graphene Composites with Excellent Electrochemical Performances for Lithium Ion Batteries,” *ACS Nano* **5**, 4720–4728 (2011).

¹⁵ Drew Edelberg, Daniel Rhodes, Alexander Kerelsky, Bumho Kim, Jue Wang, Amirali Zangiabadi, Chanul Kim, Antony Abhinandan, Jenny Ardelean, Micheal Scully, Declan Scullion, Lior Embon, Rui Zu, Elton J. G. Santos, Luis Balicas, Chris Marianetti, Katayun Barmak, Xiaoyang Zhu, James Hone, and Abhay N. Pasupathy, “Approaching the Intrinsic Limit in Transition Metal Diselenides via Point Defect Control,” *Nano Letters* **19**, 4371–4379 (2019).

¹⁶ Liang Cai, Jingfu He, Qinghua Liu, Tao Yao, Lin Chen, Wensheng Yan, Fengchun Hu, Yong Jiang, Yidong Zhao, Tiandou Hu, Zhihu Sun, and Shiqiang Wei, “Vacancy-Induced Ferromagnetism of MoS₂ Nanosheets,” *Journal of the American Chemical Society* **137**, 2622–2627 (2015).

¹⁷ Chunxu Bai, Yanling Yang, and Lin Bai, “Giant magnetoresistance control and nontrivial metallic state manipulation in a transition-metal dichalcogenide spin-valve using a gate voltage,” *Journal of Physics: Condensed Matter* **30**, 495801 (2018).

¹⁸ Felipe Crasto de Lima and Adalberto Fazzio, “At the Verge of Topology: Vacancy-Driven Quantum Spin Hall in Trivial Insulators,” *Nano Letters* **21**, 9398–9402 (2021).

¹⁹ Hao Qiu, Tao Xu, Zilu Wang, Wei Ren, Haiyan Nan, Zhenhua Ni, Qian Chen, Shijun Yuan, Feng Miao, Fengqi Song, Gen Long, Yi Shi, Litao Sun, Jinlan Wang, and Xinran Wang, “Hopping transport through defect-induced localized states in molybdenum disulphide,” *Nature Communi-*

- cations **4**, 2642 (2013).
- ²⁰ Moh. Adhib Ulil Absor, Iman Santoso, Harsojo, Kamsul Abraha, Fumiyuki Ishii, and Mineo Saito, “Defect-induced large spin-orbit splitting in monolayer PtSe₂,” *Phys. Rev. B* **96**, 115128 (2017).
- ²¹ P. Hohenberg and W. Kohn, “Inhomogeneous Electron Gas,” *Phys. Rev.* **136**, B864–B871 (1964).
- ²² W. Kohn and L. J. Sham, “Self-Consistent Equations Including Exchange and Correlation Effects,” *Phys. Rev.* **140**, A1133–A1138 (1965).
- ²³ John P. Perdew, Kieron Burke, and Matthias Ernzerhof, “Generalized Gradient Approximation Made Simple,” *Phys. Rev. Lett.* **77**, 3865–3868 (1996).
- ²⁴ Stefan Grimme, Jens Antony, Stephan Ehrlich, and Helge Krieg, “A consistent and accurate ab initio parametrization of density functional dispersion correction (DFT-D) for the 94 elements H-Pu,” *The Journal of Chemical Physics* **132**, 154104 (2010).
- ²⁵ Stefan Grimme, Stephan Ehrlich, and Lars Goerigk, “Effect of the damping function in dispersion corrected density functional theory,” *Journal of Computational Chemistry* **32**, 1456–1465 (2011).
- ²⁶ P. E. Blöchl, “Projector augmented-wave method,” *Phys. Rev. B* **50**, 17953–17979 (1994).
- ²⁷ G. Kresse and D. Joubert, “From ultrasoft pseudopotentials to the projector augmented-wave method,” *Phys. Rev. B* **59**, 1758–1775 (1999).
- ²⁸ G. Kresse and J. Hafner, “Ab initio molecular dynamics for open-shell transition metals,” *Phys. Rev. B* **48**, 13115–13118 (1993).
- ²⁹ G. Kresse and J. Furthmüller, “Efficient iterative schemes for ab initio total-energy calculations using a plane-wave basis set,” *Phys. Rev. B* **54**, 11169–11186 (1996).
- ³⁰ Bruno Focassio, Gabriel R. Schleder, Felipe Crasto de Lima, Caio Lewenkopf, and Adalberto Fazzio, “Amorphous Bi₂Se₃ structural, electronic, and topological nature from first principles,” *Phys. Rev. B* **104**, 214206 (2021).